Electronic Reconstruction of α-Ag_2WO_4 Nanorods for Visible-Light Photocatalysis

Zhaoyong Lin,[†] Jiling Li,[†] Zhaoqiang Zheng, Jiahao Yan, Pu Liu, Chengxin Wang, and Guowei Yang*

State Key Laboratory of Optoelectronic Materials and Technologies, Nanotechnology Research Center, School of Materials Science & Engineering, School of Physics & Engineering, Sun Yat-sen University, Guangzhou 510275, Guangdong, People's Republic of China. [†]Z. Lin and J. Li contributed equally to this work.

ABSTRACT α-Ag_2WO_4 (AWO) has been studied extensively due to its H_2 evolution and organic pollution degradation ability under the irradiation of UV light. However, the band gap of AWO is theoretically calculated to be 3.55 eV, resulting in its sluggish reaction to visible light. Herein, we demonstrated that, by using the electronic reconstruction of AWO nanorods upon a unique process of laser irradiation in liquid, these nanorods performed good visible-light photocatalytic organics degradation and H_2 evolution. Using commercial AWO powders as the starting materials, we achieved the electronic reconstruction of AWO by a recrystallization of the starting powders upon laser irradiation in liquid and synthesized AWO nanorods. Due to the weak bond energy of AWO and the far from thermodynamic equilibrium process created by laser irradiation in liquid, abundant cluster distortions, especially [WO_6] cluster distortions, are introduced into the crystal lattice, the defect density increases by a factor of 2.75, and uneven intermediate energy levels are inset into the band gap, resulting in a 0.44 eV decrease of the band gap, which modified the AWO itself by electronic reconstruction to be sensitive to visible light without the addition of others. Further, the first-principles calculation was carried out to clarify the electronic reconstruction of AWO, and the theoretical results confirmed the deduction based on the experimental measurements.

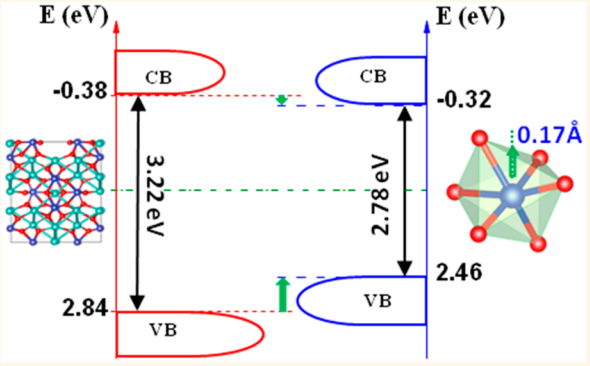

KEYWORDS: visible-light photocatalysis · organics degradation · H_2 evolution

Photocatalysis is being considered more and more for the production of green energy and degradation of environmentally hazardous substances because of the growing attention to energy and the environment all over the world.[1] TiO_2, as a typical photocatalyst, is confronted with its inherent drawback, namely, low solar energy utilization, due to its wide band gap, which ranges from 3.0 to 3.2 eV.[2] Therefore, photocatalysts sensitive to visible light are more desired for practical applications. Among them, WO_3 has been studied most extensively due to its narrow band gap of 2.7 eV and high stability.[3] Unfortunately, as a result of its unsuitable conduction band position (0.74 eV *vs* NHE), below the H^+/H_2 potential level, WO_3 cannot be used as a visible-light photocatalyst for H_2 evolution. Polyoxometalates exhibit novel physical and chemical properties on account of their excellent structure-directing effect.[4] Their electronic structures and energy band structures are believed to be modifiable and tunable through substituting their metal cations and changing their crystal structures.[5] Therefore, ternary transition metal tungstates[6,7] come into notice to modulate the WO_3 conduction band for H_2 evolution. α-Ag_2WO_4 (AWO) has been studied mostly due to its weak crystal field[8] and was verified to show H_2 evolution[9] and organic pollution degradation ability under irradiation with UV light.[10,11] However, the band gap of AWO is theoretically calculated to be 3.55 eV, resulting in its sluggish reaction to visible light,[12] like TiO_2. Thereupon, many efforts have been devoted to make AWO sensitive to visible light, including its combination with sensitizers, *i.e.*, Zn−Cr, Ag_2S, Ag/AgCl, and Ag.[13−16] Unfortunately, AWO itself has not yet been been modified to be sensitive to visible light.

* Address correspondence to stsygw@mail.sysu.edu.cn.

Received for review April 7, 2015 and accepted June 10, 2015.

Published online June 10, 2015
10.1021/acsnano.5b02077

AWO is believed to consist of octahedral [WO_6], deltahedral [AgO_7], octahedral [AgO_6], tetrahedral [AgO_4], and angular [AgO_2] clusters, in which O−Ag−O and O−W−O bonds have a weak interaction. Therefore, the relative positions of O, W, and Ag atoms are usually variable, resulting in the variation of bond lengths and bond angles. Due to the structure-directing and spontaneous polarization properties of AWO, such distortions in the cluster will lead to the variation of cluster electronic density and the energy band structure.[17,18] It is worth mentioning that the degree of cluster distortions in AWO materials depends on the synthetic methods and conditions. Laser ablation in liquid (LAL) is a promising technique for preparing metastable and defective materials because of the far from thermodynamic equilibrium process in the generated plasma plumes.[19−21] Many functional nanomaterials and nanostructures have been fabricated successfully by LAL for practical application in recent years.[22−24] Thus, LAL can be expected to realize the goal of modifying AWO itself to be sensitive to visible light.

For the above-mentioned issues, in this contribution, we report that defective AWO nanorods with abundant cluster distortions are prepared by LAL. Defect density is calculated to increase by a factor of 2.75, and uneven intermediate energy levels are demonstrated to be inset into the forbidden band, resulting in a 0.44 eV decrease of the band gap,[25] which is further supported by the first-principles calculation. Its energy band is verified to be suitable for visible-light photocatalysis. We also demonstrate that the as-prepared AWO nanorods manifest methyl orange (MO) degradation and H_2 evolution performance in the irradiation with visible light. To the best of our knowledge, this is the first time that reconstruction of the electronic structure of AWO nanorods for visible-light photocatalytic organics degradation and H_2 evolution has been achieved.

RESULTS AND DISCUSSION

Synthesis and Characterization of AWO Nanorods. Typical morphology and structure characterization results of the unirradiated and irradiated AWO samples are shown in Figure 1 and Figure 2, respectively. From SEM images of the sample before and after the pulsed laser irradiation, shown in Figure 1a and Figure 2a, clearly, we can see that both samples are thin rod-like, while the irradiated ones are more regular, uniform, and dispersed than the unirradiated ones. In detail, the unirradiated rods are of uneven size with a length ranging from 200 to 600 nm and a diameter ranging from 50 to 200 nm. They seem to aggregate severely and not in a standard shape of a rod, as seen in the inset in Figure 1a. In contrast, the irradiated sample is in an exact shape of a rod with a length of 150 nm and a diameter of 950 nm. For further knowledge of the morphology and elemental distribution, energy

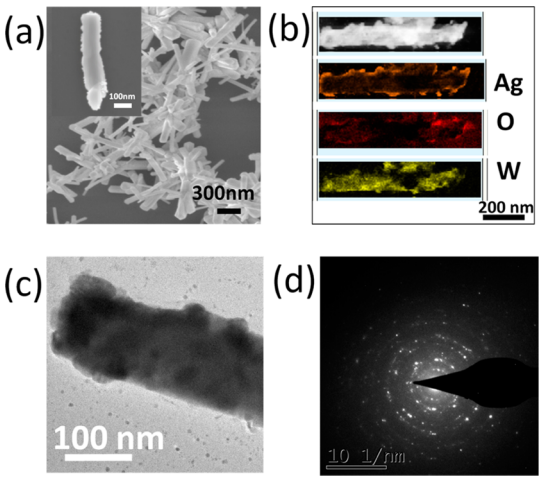

Figure 1. (a) SEM images at low and high magnification (inset), (b) EDX elemental mapping analyses, (c) TEM image, and (d) corresponding SAED pattern of the unirradiated AWO sample.

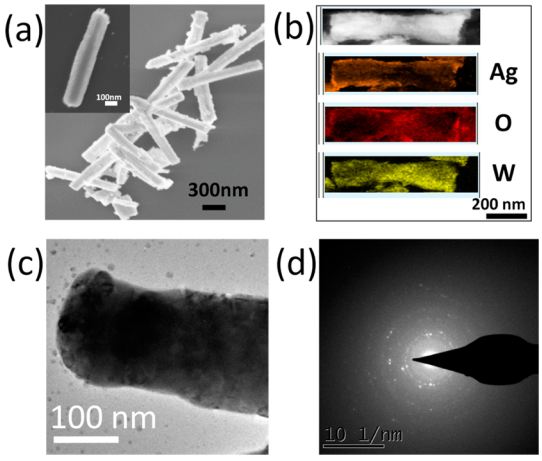

Figure 2. (a) SEM images at low and high magnification (inset), (b) EDX elemental mapping analyses, (c) TEM image, and (d) corresponding SAED pattern of the irradiated AWO sample.

dispersive X-ray (EDX) elemental mapping analyses were carried out. It is clearly visible from Figure 1b and Figure 2b that Ag, O, and W elements spread over the entire area of the samples, and the irradiated sample shows a more regular rod-like structure than the unirradiated one. TEM images in Figure 1c and Figure 2c show that there are some protuberances on the surfaces of the unirradiated AWO nanorod, while the surface of the irradiated AWO nanorod is smoother. In this situation, we believe that the laser irradiation of the original Ag_2WO_4 powders in water experiences a process of ionization and recrystallization in instantaneously high temperature and pressure in the plasma plumes resulting from the rather high power density of a nanosecond-pulsed laser, as discussed by Yang.[20] Although the morphologies and size of the original AWO nanorods are nonuniform, the ionization and recrystallization process guarantee the uniform growth

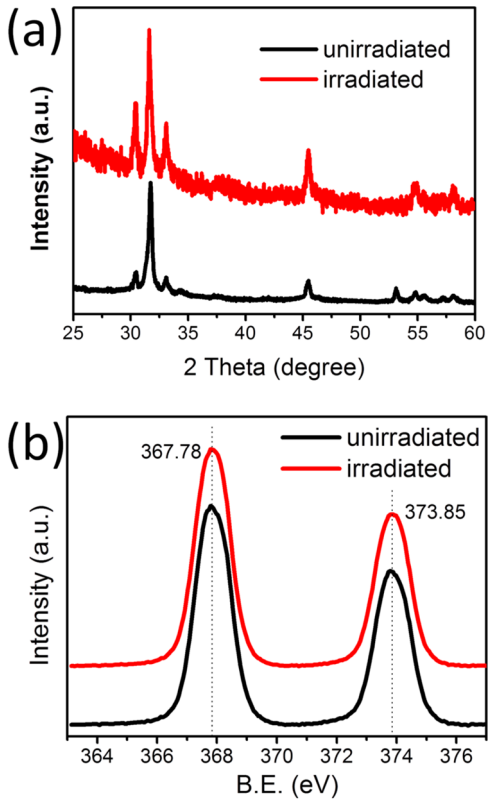

Figure 3. (a) XRD patterns and (b) high-resolution Ag element XPS spectra of the unirradiated and irradiated AWO samples.

of the final AWO nanorods. The SAED patterns are shown in Figure 1d and Figure 2d. Note that the diffraction spots of the unirradiated sample are sharp and bright, while those of the irradiated sample are dispersive and dim. The crystallinity of the irradiated AWO crystals seems to be lower.

The corresponding XRD patterns in Figure 3a indicate that both of the samples have an orthorhombic structure with a space group of *Pn*2*n* and a C_{2v}^{10} symmetry (PDF#34-0061). The main peak at 2θ = 31.6° belongs to the (231) facet of α-Ag_2WO_4, and the relative intensities of different peaks of both of the samples are a little different. The signal-to-noise ratio of the irradiated sample seems to be lower, and small peaks at 2θ = 53.6°, 54.7°, and 57.2°cannot be observed in the XRD pattern of the irradiated sample, mainly because the crystallinity of the irradiated sample is lower than that of the unirradiated one. Therefore, it is notable that the order degree of the commercial AWO crystal could be diminished by LAL.[26] Since the plasma plume quenching time is extremely short (generally tens of picoseconds),[20] the recrystallization process of AWO is exceedingly rapid and defects may be frozen and introduced into the crystal lattice. Zeng *et al.* believed that the introduction of defects in the LAL process originates from the far from thermodynamic equilibrium conditions, reactant-rich environment, and rapid recrystallization rate, which is coincident with our case.[27] Still, the diffraction peaks of both samples are sharp and well-defined, indicating that they are structurally ordered at long range. In addition, according to the previous report, AWO is sensitive to electromagnetic radiation,[28] and local amorphization may exist in AWO nanorods in this LAL procedure, resulting from the local Ag^+ reduction and Ag filament growth.[16,29]

High-resolution XPS of Ag element was carried out to examine its chemical state, as shown in Figure 3b. Both of the Ag 3d spectra of samples before and after laser irradiation consist of two individual peaks at 367.78 and 373.85 eV, which are highly symmetric. They are believed to be Ag $3d_{5/2}$ and Ag $3d_{3/2}$ binding energies of Ag^I, respectively, not apparent existing Ag^0 XPS peaks.[30] There is no obvious difference between the two XPS spectra, and we can conclude that the chemical states of the AWO samples before and after laser irradiation are constant. Moreover, no Ag diffraction peaks can be observed in the XRD patterns. Therefore, we can deny the assumption that laser irradiation would result in Ag filament growth and crystallinity decline on this issue. In view of the long-range structural order and order degree decline, the defects may exist in their own crystal lattice at short range or intermediate range.

Raman vibrational phonon mode spectrum characterization is a powerful and effective technology to investigate the structural ordering and symmetry at short range (see Figure 4a). There are 18 and 11 active modes recognizable in the Raman spectra of AWO samples before and after laser irradiation, respectively, marked by purple dotted lines. This indicates the long-range order of both samples, identical to the XRD patterns. Roughly, the active modes between 1000 and 500 cm^{-1} can be assigned to the vibration in [WO_6] clusters, while the ones from 500 to 100 cm^{-1} can be assigned to external vibrational modes of [AgO_7], [AgO_6], [AgO_4], and [AgO_2] clusters.[31] Especially, the main mode at 884 cm^{-1} is the symmetric stretching of O−W−O bonds in [WO_6] clusters.[12] Comparing the two Raman spectra, we can clearly see that the modes of the irradiated AWO sample are much broader than those of the unirradiated ones and a small shift between them, indicating structural disorder at short range in the irradiated AWO sample. The symmetric stretching of O−W−O bonds in [WO_6] clusters of the irradiated AWO sample at 884 cm^{-1} is asymmetric and broad, showing that there may be a different degree of distortion in the [WO_6] clusters.

In order to verify the [WO_6] cluster distortions, FTIR analyses were carried out, which provide information on structural ordering in O−W−O bonds in the range from 1000 to 325 cm^{-1}, shown in Figure 4b. The intense absorption bands at 827 and 862 cm^{-1}, ascribed to the asymmetric stretching vibrations of the O−W−O bonds, can be observed in both samples.

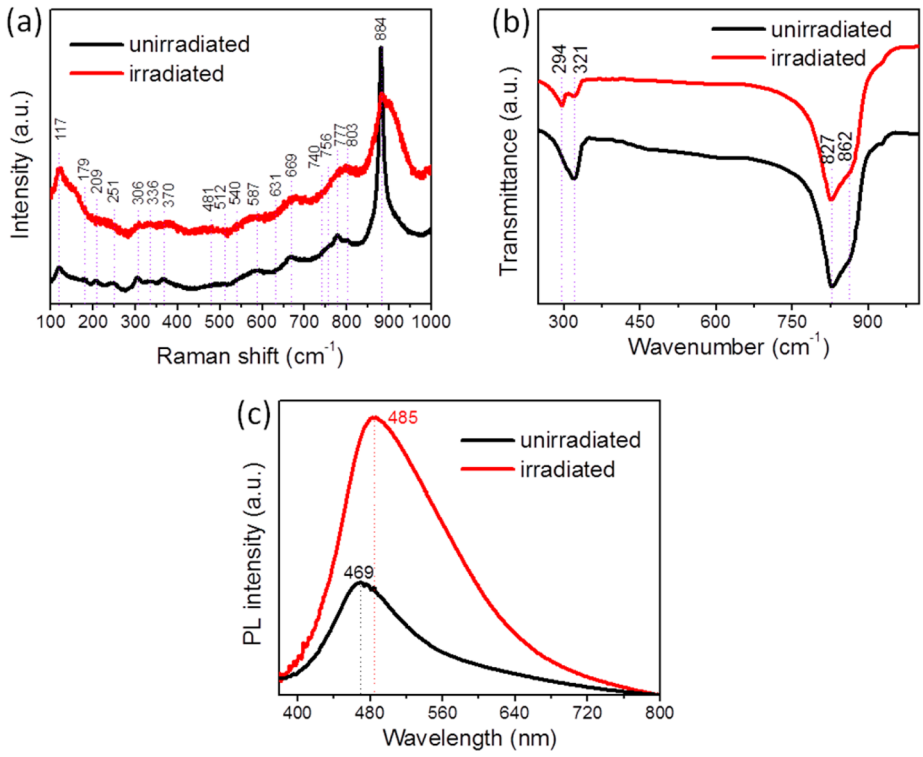

Figure 4. Cluster distortion characterization of the unirradiated and irradiated AWO samples. (a) Raman spectra, (b) FTIR spectra, (c) PL spectra.

The bands identified at 321 and 294 cm^{-1} are related to the symmetric bending vibrations and torsional motion in [WO_6] clusters, respectively.[17] Besides, the external band at 930 cm^{-1} of the O–C–O bond stretching mode is also found in both of the FTIR spectra, which may be derived from the dissolved carbon dioxide in the water used in the synthetic process.[32] Both of the samples can be verified to have [WO_6] cluster distortions in their crystal lattices. However, the degree of cluster distortions in these two samples seems to be different since the torsional motion mode can be detected only in the irradiated sample.

At this point, the characteristic of long-range order and short-range disorder with abundant cluster (especially [WO_6] clusters) distortions is demonstrated in the irradiated AWO sample. Thus, it is time to determine the defect density of the AWO sample, which will have a great influence on their physical and chemical properties. Photoluminescence is a physical process involving the electronic structure of the sample at intermediate range, which could be used to determine the defect density of AWO in our case. Both the unirradiated and irradiated AWO samples were deposited onto clean silicon wafers and excited by a laser with a wavelength of 325 nm to detect their PL properties (see Figure 4c). Both of the samples show PL emission from 380 to 800 nm. Since the band gap of AWO is theoretically calculated to be 3.55 eV (349 nm), the PL process would refer to the participation of intermediate energy levels in the band gap, resulting from the cluster distortions and defects. The irradiated AWO sample exhibits stronger PL emission than the unirradiated one. The width ratio and height ratio of the two PL emission peaks are determined to be 1.11 and 2.47, respectively. Thus, the PL emission peak area ratio is calculated as 2.75. We can make an equivalent conclusion that the defect density ratio of the irradiated and unirradiated AWO samples is 2.75. PL emission at 469 or 485 nm is ascribed to charge transfer from distorted [WO_6] clusters to undistorted [WO_6] clusters.[17] Clearly, we can see that the PL emission peak shows a 16 nm right shift and the peaks seem to be asymmetric, which may be related to the energy band structures of the samples. Therefore, UV–vis diffuse reflectance spectroscopy (DRS) (Figure 5a,b) and valence-band X-ray photoemission spectroscopy (VB XPS) (Figure 5c) were carried out to confirm the energy band structures.

The unirradiated sample shows a band-edge absorption at 400 nm, typical for AWO with a wide band gap. In contrast, the irradiated sample shows obvious visible light absorption from 400 to 700 nm because of the abundant defects. The band gaps of samples can be calculated to be 3.22 and 2.78 eV, respectively (see Figure 5b).[33] The valence band (VB) positions of samples are determined to be 2.84 and 2.46 eV (*vs* NHE) by linear extrapolation of the leading edges of VB XPS spectra to the base lines (see Figure 5c), respectively. Thus, the conduction band (CB) positions of the two samples can be calculated as −0.38 and −0.32 eV (*vs* NHE), respectively. Apparently, the narrowing of

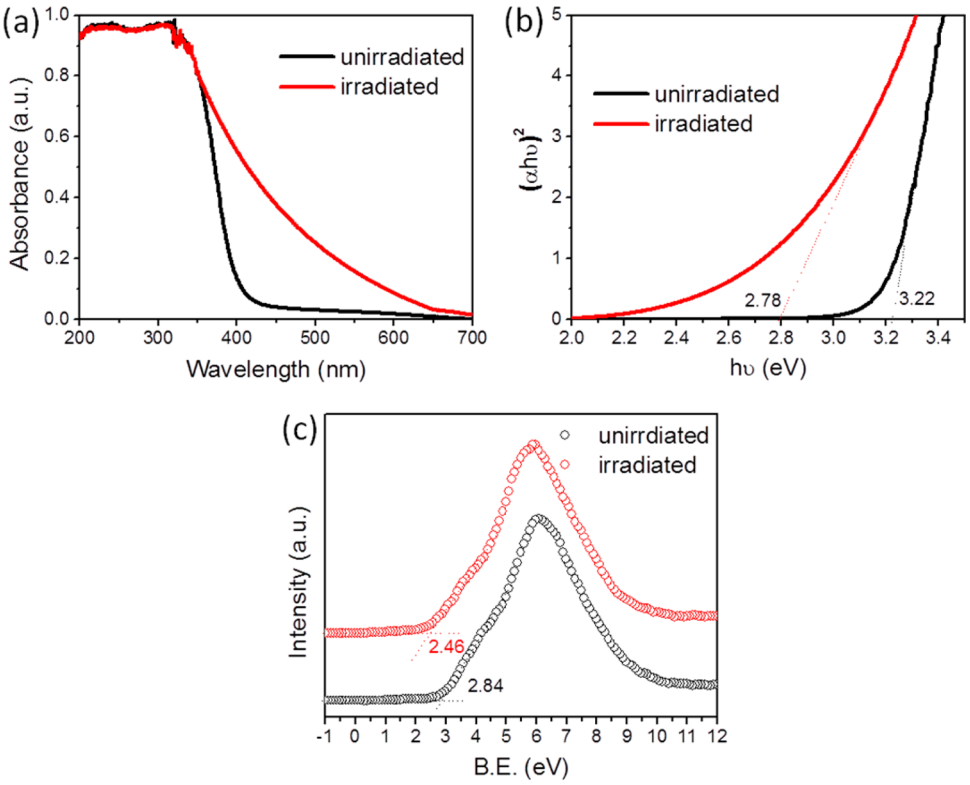

Figure 5. Energy band structure characterization of the unirradiated and irradiated AWO samples. (a) UV−vis adsorption spectra, (b) Tauc plots, and (c) VB XPS spectra.

the band gap is due to the introduction of abundant intermediate energy levels within the band gap. As the band gap narrows, the occurrence of cluster-to-cluster charge transfer is more likely; in addition, the introduction of abundant defects will lead to stronger electronic polarization between clusters. For the two reasons above, a stronger PL emission of the irradiated AWO samples would occur.[17] As for the asymmetry of the PL emission peaks, it may be due to the uneven distribution of intermediate energy levels within the band gap, resulting from the different degrees of distortion in different [WO_6] clusters.

From the above-mentioned issues, we can conclude that regular, uniform, and dispersive AWO nanorods are prepared by a process involving laser irradiation of AWO powders in water. Due to the instantaneously high temperature and pressure in the plasma plumes, AWO powders experience a process of ionization and recrystallization with a very rapid kinetics, and abundant cluster distortions,[34] especially [WO_6] cluster distortions, are introduced into the crystal lattice. The sample is demonstrated to be long-range ordered and short-range disordered by SAED, XRD, Raman, and FTIR analyses. The defect density increases by a factor of 2.75 due to the introduction of abundant cluster distortions, which strengthens the photoluminescence (PL) emission and narrows the band gap by a value of 0.44 eV. Because of the different degrees of distortion in different [WO_6] clusters, uneven intermediate energy levels are inset into the forbidden band, resulting in asymmetric PL emission peaks. At this point, electronic reconstruction of AWO nanorods has been achieved.

Additionally, we have tried to control and adjust the defect density of the sample by tuning the laser pulse energy. However, the original AWO powders are not ionized effectively with a pulse energy lower than 120 mJ (the ablation threshold). When the pulse energy is higher than 170 mJ, the products are always in a chaotic shape, resulting from the interaction between the subsequent laser pulse and the previously generated plasma plume. The photocatalytic performance of such a sample is demonstrated to be rather poor. Therefore, we can adjust the defect density of the sample by tuning the laser pulse energy in the range of 120 to 170 mJ. For example, a maximum decrease of 0.44 eV of the band gap can be obtained with a pulse energy of 150 mJ. Meanwhile, a minimum decrease of 0.42 eV can be obtained with a pulse energy of 120 mJ. Further efforts for controlling the defect density are required in our subsequent work.

First-Principles Calculation. As mentioned above, [WO_6] cluster distortions originating from the variation of the relative atom position would correspondingly lead to the variation of the electronic properties of AWO. To confirm this deduction, we perform the first-principles calculation on the electronic structure of the pristine bulk AWO and its specific [WO_6] cluster-distortion

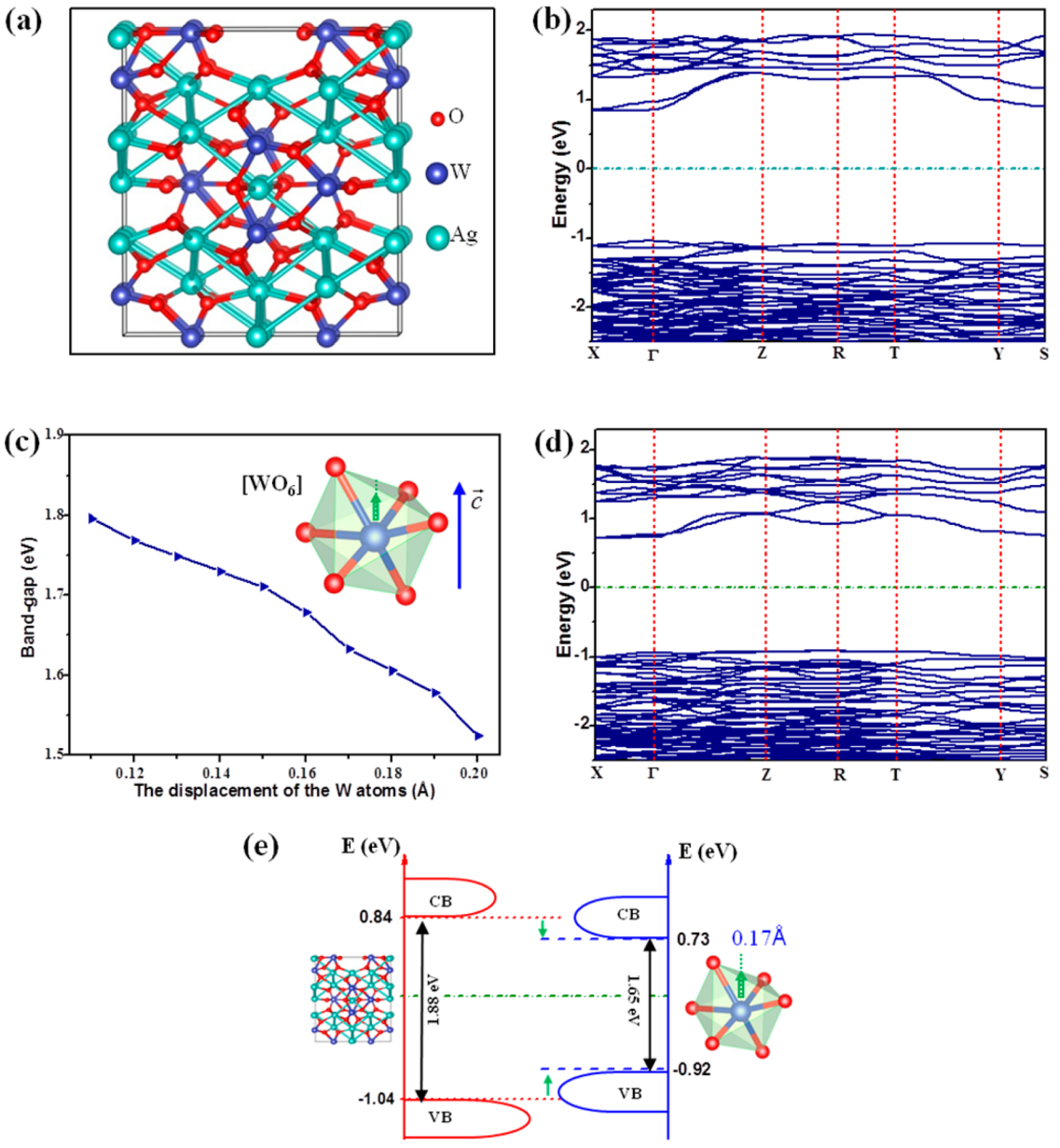

Figure 6. Geometrical and band structures of the bulk AWO and its [WO_6] cluster-distortion configurations. (a, b) Optimized equilibrium configuration and band structure of the pristine bulk AWO, respectively. (c) Curve of the band gap with respect to the displacement of the W atom along vector $\vec{c}$ of the bulk AWO lattice. The inset is the schematic map of the shift of the W atom in the octahedral [WO_6] along $\vec{c}$. (d) Band structure of the specific [WO_6] cluster distortion with a displacement of the W atom of 0.17 Å. (e) Sketch map of the band structure involving the CB and VB, of both the pristine bulk AWO and the [WO_6] cluster-distortion configuration with a displacement of 0.17 Å. The Fermi level is denoted by the green dotted line and set to zero.

configurations. In this case, the electronic structure of the bulk AWO is seen as approximately comparable with those of our present samples of the unirradiated AWO nanorods since they have a cross section of 100 nm. All the theoretical calculations are performed using the DMOL^3 package.[35,36] The generalized gradient approximation (GGA) with the Perdew–Burkle–Ernzerhof (PBE) exchange–correlation function is employed without spin unrestricted. The atomic orbital basis set is of double-numerical quality with inclusion of polarization functions (DNP). The configurations are fully relaxed with the *Pn*2*n* symmetric constraints until the maximal forces and displacement are less than 0.002 hartree/Å and 0.005 Å. The Kohn–Sham equations are solved self-consistently with a convergence of 10^{-5} Ha (1 Ha = 27.2114 eV) on the total energy.

First, the geometrical structure of the pristine bulk AWO is constructed and optimized. The equilibrium configuration is obtained and shown in Figure 6a. The lattice parameters of the optimized AWO are $\vec{a}$ = 10.915 Å, $\vec{b}$ = 12.638 Å, and $\vec{c}$ = 5.943 Å, in good agreement with those of our experimental observation and the previous literature.[17] As shown in Figure 6a, the bulk AWO consists of octahedral [WO_6] and

polyhedral [AgO_x] clusters (x = 2, 4, 6, 7), with Ag atoms and W atoms both surrounded by O atoms through forming O−Ag−O and O−W−O bonds, respectively. The electronic structure of the pristine bulk AWO is then investigated as shown in Figure 6b. Clearly, we can see that the band structure is of typical direct band gap and semiconductor character with the calculated band gap of 1.88 eV. This value is smaller than the experimental values of 3.22 eV due to the well-known shortcoming of density functional theory (DFT) in describing the excited states. Correspondingly, DFT calculations always underestimate the band gaps of materials. Therefore, the value of the band gap obtained from the present calculations is also underestimated. However, the relative value between that of the pristine and distorted AWO both from DFT calculations is comparable and has the same significance.

As known, the weak interaction between O−Ag−O and O−W−O bonds in the bulk AWO suggests that the relative atom positions of O, W, and Ag atoms are usually variable, with the variation of incidental relative displacement and bond lengths between atoms. Consequently, distortions originating from the variation of the relative atom position would correspondingly lead to the variation of the electronic properties and band structure of the bulk materials. On the basis of our experimental analysis, the cluster distortions most probably happened upon the displacement of the W atom in the [WO_6] cluster. Considering the *Pn*2*n* symmetric characteristic of the bulk AWO, in the following cluster-distortion simulations, the W atoms will be manually shifted only along the lattice vector $\vec{c}$, with a displacement interval of 0.01 Å from 0.10 to 0.20 Å. In order to explore the relationship of the distortions and electronic properties, the band structures of all these single-point configurations are then investigated.

Figure 6c gives the curve of the band gaps along with the displacement of the W atom from the equilibrium position in the optimized configuration along the vector $\vec{c}$ of the AWO crystal lattice. Herein, the inset is the sketch map of the W atom moving from the equilibrium position in the octahedral [WO_6] cluster. These results obviously indicate that the band gap of AWO is greatly tuned by the structural distortion from the shift of the W atom in the [WO_6] and monotonically decreased with the increasing displacement of the W atom. As a representative, the band structure of the distorted AWO with the W atom shifted 0.17 Å is further deliberated. Compared with that of the pristine AWO, the band gap of the distorted AWO is decreased to 1.65 eV, as shown in Figure 6d. To lend further insight into this tuned electronic characteristic, the structures of the CB and VB of the distorted AWO are investigated. The results are schematically shown in Figure 6e. As seen, the bottom of the CB (BCB) and the top of the VB (TVB) of the bulk AWO are 0.84 eV and −1.04 eV, respectively. However, when the displacement of the W atom along $\vec{c}$ is 0.17 Å, the BCB and TVB of the distorted AWO are adjusted to 0.73 eV and −0.92 eV, respectively. In contrast with those of the pristine AWO, the BCB has descended and the TVB has oppositely ascended to a certain extent. Correspondingly, the band gap of the distorted AWO is decreased from 1.88 eV of the pristine AWO to 1.65 eV. In summary, according to all the calculated results, it is obvious that the band structures from the DFT calculations are well consistent with those of our experimental analysis.

According to the experiments and theoretical calculations, we can clearly see that the band structure of the AWO nanorod could be adjusted using a unique process of laser irradiation in liquid. The band structure of the irradiated AWO samples seems to be suitable for the visible-light photocatalytic organics degradation and H_2 evolution. In addition, the strong PL performance indicates the excellent photogenerated electron−hole pair separation ability, which is critical for the photocatalytic activity. Therefore, the distorted AWO nanorods are used as photocatalysts in the following experiments.

Visible-Light Photocatalysis. The visible-light photocatalytic MO degradation experiments are shown in Figure 7a−c. The characteristic absorption peak of MO at 464 nm decreases rapidly. According to the Beer−Lambert law,[21] the concentration of MO solution is proportional to the normalized absorbance, shown in Figure 7a. Therefore, the relative concentration variation of MO solution is plotted in Figure 7b, indicating that about 90% of MO molecules were degraded in the presence of the irradiated AWO sample, while the concentration of MO solution shows no obvious variation in the presence of the unirradiated AWO sample. Assuming that the degradation process obeys first-order kinetics ($C = C_0e^{-kt}$, k is the photodegradation rate), the plots of $-\ln(C/C_0)$ as a function of irradiation time t are shown in Figure 7c. The photodegradation rate k can be estimated to be 0.185 min^{-1} by the slope of the plot. Note that the photodegradation rate in the presence of the unirradiated AWO sample is nearly zero. Compared with the unirradiated AWO sample, the irradiated one exhibits high visible-light photodegradation performance.

In consideration of the narrow band gap (2.78 eV) and the suitable conduction band position (−0.32 eV *vs* NHE), the irradiated AWO sample is believed to be qualified for H_2 evolution under the irradiation of visible light. The photocatalytic H_2 evolution activity of both of samples was carried out for 5 h, and the time course of H_2 evolution is shown in Figure 7d. The H_2 evolution rate R in the presence of the irradiated AWO sample is calculated to be 1.373 μmol h^{-1} (13.73 μmol $h^{-1}g^{-1}$), while there is no H_2 detectable in the presence of the unirradiated AWO sample.

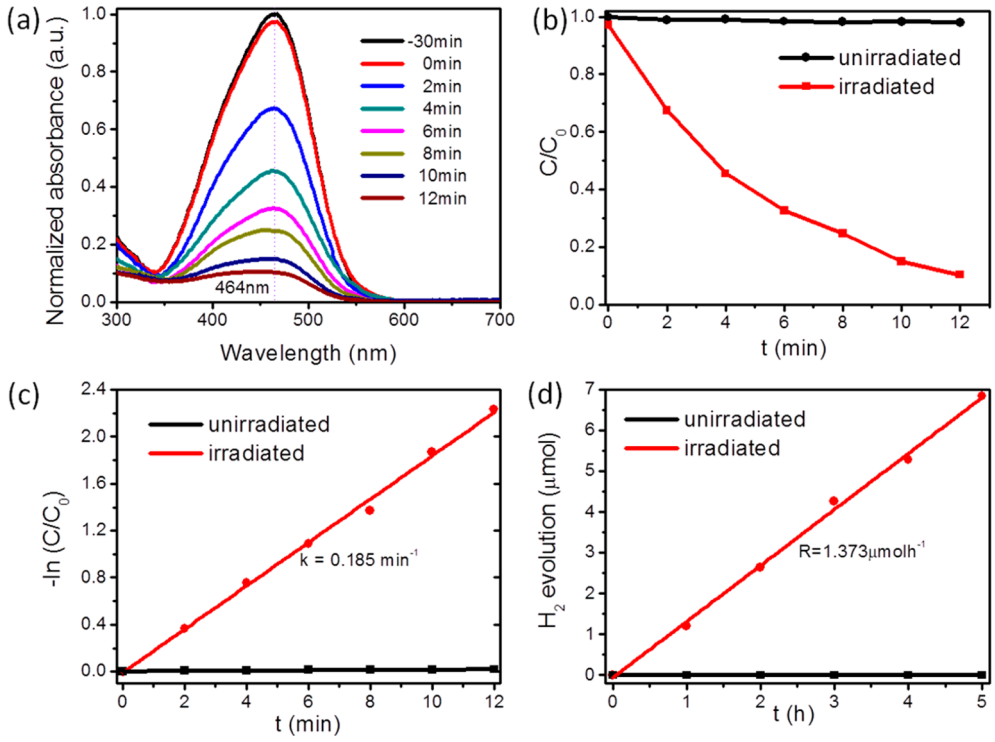

Figure 7. Visible-light photocatalysis of the unirradiated and irradiated AWO samples. (a) Typical UV−vis spectral changes of MO solution (characteristic wavelength is set as 464 nm). (b) Relative concentration variation plots of MO solution. (c) Plots of $-\ln(C/C_0)$ *vs t* in MO solution. (d) Typical time course of H_2 evolution from water under visible-light irradiation.

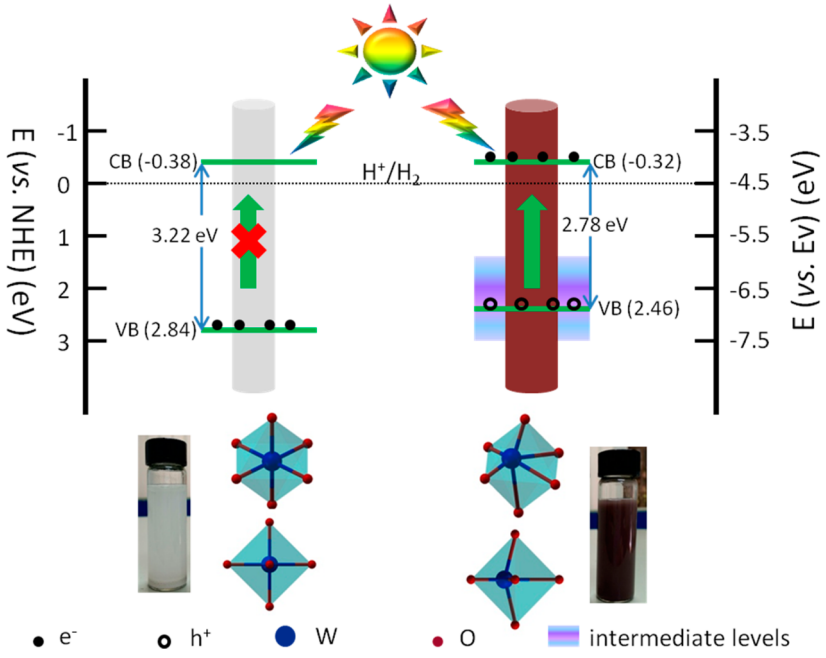

Figure 8. Schematic illustration of the visible-light photocatalytic mechanism based on the band gap narrowing because of cluster distortions and intermediate energy levels. The four $[WO_6]$ cluster ball-and-stick model schemes are the front and top views in the AWO samples before and after LAL, respectively.

The visible-light photocatalytic mechanism for MO degradation and H_2 evolution is sketched in Figure 8. During the recrystallization of AWO powders under the irradiation of a pulsed laser in water, different degrees of cluster distortions are kept in the AWO crystals and uneven intermediate energy levels are inset into the band gap, resulting in a 0.44 eV decrease of the band gap and an allochromasia of the suspension (see the photographs in Figure 8). Under visible light irradiation, the unirradiated sample cannot absorb photons and no electron−hole (e^-−h^+) pairs are generated, and it shows no photocatalytic performance. In

contrast, the irradiated sample can absorb visible light effectively, and electrons migrate to the conduction band while holes leave in the valence band. In the degradation experiments, the generated $e^- - h^+$ pairs would react with the surrounding substances to generate reactive species with powerful reduction or oxidation ability and further degrade the MO molecules. In the H_2 evolution experiments, the generated holes would be consumed by the methanol molecules and the remaining electrons in the conduction band would reduce the H^+ in the solution to H_2 with the help of cocatalyst Pt.[37]

Although visible-light photocatalytic organics degradation and H_2 evolution performance was demonstrated, the yield of H_2 was relatively low. A possible reason is that AWO nanorods are regarded as a single photocatalyst for H_2 evolution. A nanocomposite is an alternative to enhance photocatalysis in the visible light range. In detail, it is very common and effective for AWO to be combined with noble metal nanomaterials, such as Au, Ag, Pd, and Au−Ag alloy. Homojunction fabrication by combining α-Ag_2WO_4 with β-Ag_2WO_4 may be an exciting project. Moreover, TiO_2, ZnO, and Cu_2O are typical photocatalysts, and it is desirable to prepare a heterojunction with them. In addition, narrow-band-gap and up-conversion nanomaterials may be valid to be combined with the as-prepared AWO nanorod to enhance its photocatalytic activity, such as Fe_2O_3, carbon quantum dots, and rare-earth materials.

CONCLUSION

In summary, the electronic reconstruction of α-Ag_2WO_4 nanorods for visible-light photocatalytic organics degradation and H_2 evolution has been accomplished in this work. Due to the weak bond energy in α-Ag_2WO_4 and the instantaneously high temperature and pressure of a LAL procedure, abundant cluster distortions, especially [WO_6] cluster distortions, are introduced into the crystal lattice. The defect density increases by a factor of 2.75, and uneven intermediate energy levels are inset into the band gap, resulting in a 0.44 eV decrease of the band gap. Modifying α-Ag_2WO_4 itself by electronic reconstruction to be sensitive to visible light without the addition of others has been realized. Moreover, visible-light photocatalytic organics degradation and H_2 evolution performance were demonstrated, and a possible visible-light photocatalytic mechanism was put forward. These results provided new insights into silver tungstate photocatalyst and energy band engineering for visible-light photocatalytic organics degradation and water photolysis.

METHODS

AWO Nanorod Synthesis. The experiments were carried out by a LAL process. Typically, 20.0 mg of white Ag_2WO_4 powders (Alfa Aesar, 99%) was put into an 18 mL glass bottle, and 12 mL of deionized water was added. After ultrasonic oscillating for 20 min to disperse the powders adequately in the water, the suspension was stirred with a magnetic stirrer. Then a second harmonic produced by a Q-switched Nd:YAG laser device with a wavelength of 532 nm, laser pulse power of 150 mJ, pulse width of 10 ns, and repeating frequency of 50 Hz was focused by a lens (200 mm) into the suspension for 50 min until a deep red colloidal solution was synthesized with no obvious solid particles suspended.

Material Characterization. The morphology of the products was observed by a thermal FE environment scanning electron microscope (SEM, Quanta 400, FEI Company). Energy dispersive X-ray elemental mapping analyses, transmission electron microscopy (TEM), and selected area electron diffraction (SAED) were recorded by an FEI Tecnai G2 F30 transition electron microscope with a field-emission gun. The products were structurally characterized by X-ray diffraction (XRD) patterns using an X-ray diffractometer (D/MAX-2200, Rigaku) under a voltage of 40 V and a current of 26 mA and recorded with a speed of 1° min^{-1} in the 2θ range 25° to 60°. Raman measurements were recorded using an inVia Raman microscope (Renishaw, England) with a He−Ne laser with a wavelength of 632.81 nm and maximum output power of 6 mW operating at 1000−100 cm^{-1}. Fourier transform infrared (FTIR) spectroscopy was recorded in the range from 1000 to 250 cm^{-1} using an FTIR spectrometer (Nicolet6700, Thermo Scientific, USA). Photoluminescence measurement was performed using an inVia Reflex microscope (Renishaw, England) with a He−Cd laser with a wavelength of 325 nm and maximum output power of 200 mW operating at 380 to 800 nm. UV−vis diffuse reflectance spectra were recorded on a UV−vis−NIR spectrophotometer (Lambda950, PerkinElmer Company) using $BaSO_4$ as a reference. High-resolution X-ray photoelectron spectroscopy and valence band XPS of samples were measured on an XPS scanning microprobe spectrometer (Escalab 250, Thermo-VG Scientific, England, Al Kα) with respect to the position of the C 1s peak at 284.6 eV.

Photocatalytic MO Degradation. MO was selected as the target pollutant. Typically, 20.0 mg of sample was added to 20 mL of MO solution (10 mg L^{-1}) in a test tube. The suspension was then stirred vigorously in the dark for 30 min to establish an adsorption−desorption equilibrium. The photodegradation test was conducted in a photochemical reaction instrument (Qiqian-III, Qiqian Company, China) using a 300 W Xe lamp with a 420 nm cutoff filter as the light source to simulate sunlight. A 2.0 mL portion of solution was drawn at every 2 min and then centrifuged at 8000 rpm for 20 min to remove the samples. Supernatants were transferred to a quartz cuvette for measuring absorption spectra using a UV−vis−NIR spectrophotometer (Lamda900, PerkinElmer). The degradation experiment of the original Ag_2WO_4 powders was carried out in the same way.

Photocatalytic H_2 Evolution. The photocatalytic H_2 evolution reactions were carried out with 100.0 mg of sample suspended in 100 mL of 20% methanol aqueous solution (20 mL of methanol and 80 mL of H_2O) in a top-irradiation-type Pyrex glass cell connected to a closed gas-circulation system at room temperature. After being thoroughly degassed for 30 min, the suspension was irradiated by a Xe lamp with a 420 nm cutoff filter at 300 W under stirring for 5 h. The H_2 evolution experiment of the original Ag_2WO_4 powders was carried out in the same way. For both of the reactions, 1 wt % Pt was *in situ* photodeposited onto the photocatalysts from a 0.5 M H_2PtCl_6 aqueous solution as cocatalyst.

Conflict of Interest: The authors declare no competing financial interest.

Acknowledgment. The National Basic Research Program of China (2014CB931700) and the State Key Laboratory of Optoelectronic Materials and Technologies of Sun Yat-sen University supported this work.

REFERENCES AND NOTES

1. Kapilashrami, M.; Zhang, Y. F.; Liu, Y.-S.; Hagfeldt, A.; Guo, J. H. Probing the Optical Property and Electronic Structure of TiO_2 Nanomaterials for Renewable Energy Applications. *Chem. Rev.* **2014**, *114*, 9662–9707.
2. Fujishima, A.; Honda, K. Electrochemical Photolysis of Water at a Semiconductor Electrode. *Nature* **1972**, *238*, 37–38.
3. Ping, Y.; Galli, G. Optimizing the Band Edges of Tungsten Trioxide for Water Oxidation: A First-Principles Study. *J. Phys. Chem. C* **2014**, *118*, 6019–6028.
4. Zhan, C. H.; Cameron, J. M.; Gao, J.; Purcell, J. W.; Long, D.-L.; Cronin, L. Time-Resolved Assembly of Cluster-in-Cluster $\{Ag_{12}\}$-in-$\{W_{76}\}$ Polyoxometalattes under Supramolecular Control. *Angew. Chem., Int. Ed.* **2014**, *53*, 10362–10366.
5. Long, D.-L.; Tsunashima, R.; Cronin, L. Polyoxometalates: Building Blocks for Functional Nanoscale Systems. *Angew. Chem., Int. Ed.* **2010**, *49*, 1736–1758.
6. Ungelenk, J.; Speldrich, M.; Dronskowski, R.; Feldmann, C. Polyol-Mediated Low-Temperature Synthesis of Crystalline Tungstate Nanoparticles MWO_4 (M = Mn, Fe, Co, Ni, Cu, Zn). *Solid State Sci.* **2014**, *31*, 62–69.
7. Silva, L. F. D.; Catto, A. C., Jr.; Cavalcante, L. S.; Andrés, J.; Aguir, K.; Mastelaro, V. R.; Longo, E. A Novel Ozone Gas Sensor Based on One-Dimensional (1D) α-Ag_2WO_4 Nanostructures. *Nanoscale* **2014**, *6*, 4058–4062.
8. Janáky, C.; Rajeshwar, K.; Tacconi, N. R. D.; Chanmanee, W.; Huda, M. N. Tungsten-Based Oxide Semiconductors for Solar Hydrogen Generation. *Catal. Today* **2013**, *199*, 53–64.
9. Tang, J. W.; Ye, J. H. Correlation of Crystal Structures and Electronic Structrues and Photocatalytic Properties of the W-Containg Oxides. *J. Mater. Chem.* **2005**, *15*, 4246–4251.
10. Chen, H. H.; Xu, Y. M. Photoactivity and Stability of Ag_2WO_4 for Organic Degradation in Aqueous Suspensions. *Appl. Surf. Sci.* **2014**, *319*, 319–323.
11. Wang, X. F.; Fu, C.; Wang, P.; Yu, H. G.; Yu, J. G. Hierarchically Porous Metastable β-Ag_2WO_4 Hollow Nanospheres: Controlled Synthesis and High Photocatalytic Activity. *Nanotechnology* **2013**, *24*, 165602–165609.
12. Longo, E.; Volanti, D. P.; Longo, V. M.; Gracia, L.; Nogueira, I. C.; Almeida, M. A. P.; Pinheiro, A. N.; Ferrer, M. M.; Cavalcante, L. S.; Andrés, J. Toward an Understanding of the Growth of Ag Filaments on α-Ag_2WO_4 and Their Photoluminescent Properties: A Combined Experimental and Theoretical Study. *J. Phys. Chem. C* **2014**, *118*, 1229–1239.
13. Zhu, J. Y.; Fan, H.; Sun, J. C.; Ai, S. Y. Anion-Exchange Precipitation Synthesis of α-Ag_2WO_4/Zn-Cr Layered Double Hydroxides Composite with Enhanced Visible-Light-Driven Photocatalytic Activity. *Sep. Purif. Technol.* **2013**, *120*, 134–140.
14. Wang, X. F.; Zhan, S.; Wang, Y.; Wang, P.; Yu, H. G.; Yu, J. G.; Hu, C. Z. Facile Synthesis and Enhanced Visible-Light Photocatalytic Activity of Ag_2S Nanocrystal-Sensitized $Ag_8W_4O_{16}$ Nanorods. *J. Colloid Interface Sci.* **2014**, *422*, 30–37.
15. Liu, X. H.; Hu, J. L.; Li, J. J.; Hu, Y.; Shao, Y.; Yang, H. J.; Tong, G. X.; Qian, H. S. Facile Synthesis of Ag_2WO_4/AgCl Nanorods for Excellent Photocatalytic Properties. *Mater. Lett.* **2013**, *91*, 129–132.
16. Longo, V. M.; Foggi, C. C. D.; Ferrer, M. M.; Gouveia, A. F.; André, R. S.; Avansi, W.; Vergani, C. E.; Machado, A. L.; André, J.; Cavalcante, L. S.; Hernandes, A. C.; Longo, E. Potentiated Electron Transference in α-Ag_2WO_4 Microcrystals with Ag Nanofilaments as Microbial Agent. *J. Phys. Chem. A* **2014**, *118*, 5769–5778.
17. Cavalcantte, L. S.; Almeida, M. A. P.; W, A., Jr.; Tranquilin, R. L.; Longo, E.; Batista, N. C.; Mastelaro, V. R.; Li, M. S. Cluster Coordination and Photoluminescence Properties of α-Ag_2WO_4 Microcrystals. *Inorg. Chem.* **2012**, *51*, 10675–10687.
18. André, J.; Gracia, L.; Gonzalez-Navarrete, P.; Longo, V. M.; W, A., Jr.; Volanti, D. P.; Ferrer, M. M.; Lemos, P. S.; Porta, F. A. L.; Hernandes, A. C.; Longo, E. Structural and Electronic Analysis of the Atomic Scale Nucleation of Ag on α-Ag_2WO_4 Induced by Electron Irradiation. *Sci. Rep.* **2014**, *4*, 5391–5397.
19. Pan, S. S.; Lu, W.; Zhao, Y. H.; Tong, W.; Li, M.; Jin, L. M.; Choi, J. Y.; Qi, F.; Chen, S. G.; Fei, L. F.; Yu, S. F. Self-Doped Rutile Titania with High Performance for Direct and Ultrafast Assay of H_2O_2. *ACS Appl. Mater. Interfaces* **2013**, *5*, 12784–12788.
20. Yang, G. W. Laser Ablation in Liquids: Applications in the Synthesis of Nanocrystals. *Prog. Mater. Sci.* **2007**, *52*, 648–698.
21. Lin, Z. Y.; Xiao, J.; Yan, J. H.; Liu, P.; Li, L. H.; Yang, G. W. Ag/AgCl Plasmonic Cubes with Ultrahigh Activity as Advanced Visible-Light Photocatalysts for Photodegrading Dyes. *J. Mater. Chem. A* **2015**, *3*, 7649–7658.
22. Zeng, H. B.; Du, X.-W.; Singh, S. C.; Kulinich, S. A.; Yang, S. K.; He, J. P.; Cai, W. P. Nanomaterials *via* Laser Ablation/Irradiation in Liquid: A Review. *Adv. Funct. Mater.* **2012**, *22*, 1333–1353.
23. Yang, J.; Ling, T.; Wu, W.-T.; Liu, H.; Gao, M.-R.; Ling, C.; Du, X.-W. A Top-Down Straegy towards Monodisperse Colloid Lead Sulphide Quantum Dots. *Nat. Commun.* **2013**, *4*, 1695–1700.
24. Xiao, J.; Ouyang, G.; Liu, P.; Wang, C. X.; Yang, G. W. Reversible Nanodiamond-Carbon Onion Phase Transformations. *Nano Lett.* **2014**, *14*, 3645–3652.
25. Gouveia, A. F.; Sczancoski, J. C.; Ferre, M. M.; Lima, A. S.; Santos, M. R. M. C.; Li, S.; Santos, R. S.; Longo, E.; Cavalcante, L. S. Experimental and Theoretical Investigations of Electronic Structurer and Photoluminescence Properties of β-Ag_2MoO_4 Microsrystals. *Inorg. Chem.* **2014**, *53*, 5589–5599.
26. Zeng, H. B.; Cai, W. P.; Liu, P. S.; Xu, X. X.; Zhou, H. J.; Klingshirn, C.; Kalt, H. ZnO-Based Hollow Nanoparticles by Selective Etching: Elimination and Reconstruction of Metal-Semiconductor Interface, Improvement of Blue Emission and Photocatalysis. *ACS Nano* **2008**, *2*, 1661–1670.
27. Zeng, H. B.; Duan, G. T.; Li, Y.; Yang, S. K.; Xu, X. X.; Cai, W. P. Blue Luminescence of ZnO Nanoparticles Based on Non-Equilibrium Processes: Defect Origins and Emission Controls. *Adv. Funct. Mater.* **2010**, *20*, 561–572.
28. Cheng, L.; Shao, Q.; Shao, M. W.; Wei, X. W.; Wu, Z. C. Photoswitches of One-Dimensional Ag_2MO_4 (M = Cr, Mo and W). *J. Phys. Chem. C* **2009**, *113*, 1764–1768.
29. Longo, E.; Cavalcante, L. S.; Volanti, D. P.; Fouveia, A. F.; Longo, V. M.; Varela, J. A.; Orlandi, M. O.; Andrés, J. Direct *in Situ* Obeservation of the Electron-Driven Synthesis of Ag Filaments on α-Ag_2WO_4 Crystals. *Sci. Rep.* **2013**, *3*, 1676–1679.
30. Daupor, H.; Wongnawa, S. Urchinlike Ag/AgCl Photocatalyst: Synthesis, Characterizatoin and Activity. *Appl. Catal. A: Gen.* **2014**, *473*, 59–69.
31. Yan, T. J.; Li, L. P.; Tong, W. M.; Zheng, J.; Wang, Y. J.; Li, G. S. $CdWO_4$ Polymorphs: Selective Preparation, Electronic Structures, and Photocatalytic Activities. *J. Solid State Chem.* **2011**, *184*, 357–364.
32. Sczancoski, J. C.; Cavalcante, L. S.; Marana, N. L.; Silva, R. O. D.; Tranquilin, R. L.; Joya, M. R.; Pizani, P. S.; Varela, J. A.; Sambrano, J. R.; Li, M. S.; Longo, E.; Andrés, J. Electronic Structure and Optical Properties of $BaMoO_4$ Powders. *Curr. Appl. Phys.* **2010**, *10*, 614–624.
33. Xiao, J.; Wu, Q. L.; Liu, P.; Liang, Y.; Li, H. B.; Wu, M. M.; Yang, G. W. Highly Stable Sub-5 nm $Sn_6O_4(OH)_4$ Nanocrystals with Ultrahigh Activity as Advanced Photocatalytic Materials for Photodegradation of Methyl Orange. *Nanotechnology* **2014**, *25*, 135702–135711.
34. Pereira, P. F. S.; Moura, A. P. D.; Nogueira, I. C.; Lima, M. V. S.; Longo, E.; Filho, P. C. D. S.; Serra, O. A.; Nassar, E. J.; Rosa, I. L. V. Study of the Annealing Temperature Effect on the Structural and Luminescent Properties of $SrWO_4$: Eu Phosphors Prepared by a Non-Hydrolytic Sol-Gel Process. *J. Alloys Compd.* **2012**, *526*, 11–21.
35. Delley, B. From Molecules to Solids with the DMol 3 Approach. *J. Chem. Phys.* **2000**, *113*, 7756–7764.
36. Perdew, J. P.; Wang, Y. Accurate and Simple Analytic Representation of the Electron-Gas Correlation Energy. *Phys. Rev. B* **1992**, 13244–13249.
37. Yang, J. H.; Wang, D.; Han, H. X.; Li, C. Roles of Cocatalysts in Photocatalysis and Photoeletrocatalysis. *Acc. Chem. Res.* **2013**, *46*, 1900–1909.